Magnetic phases of the $S = \frac{5}{2}$ triangular-lattice antiferromagnet $RbFe(MoO_4)_2$ as determined by ultrasound velocity measurements

A. Zelenskiy,[1] J. A. Quilliam,[2] A. Ya. Shapiro,[3] and G. Quirion[4]

[1]*Department of Physics and Atmospheric Science, Dalhousie University, Halifax, Nova Scotia, Canada B3H 3J5*

[2]*Institute Quantique, Département de Physique, and RQMP, Université de Sherbrooke, Sherbrooke, Québec, Canada J1K 2R1*

[3]*A. V. Shubnikov Institute for Crystallography RAS, 119333 Moscow, Russia*

[4]*Department of Physics and Physical Oceanography, Memorial University of Newfoundland, St. John's, Canada A1B 3X7*

(Received 4 October 2020; revised 9 March 2021; accepted 26 May 2021; published 21 June 2021)

$RbFe(MoO_4)_2$ is one of the best physical examples of a quasi-two-dimensional easy-plane triangular-lattice antiferromagnet. Although the magnetic phase diagram of this material has been well-studied, there are discrepancies in the literature concerning the number of magnetic phases, as well as the nature of the phase transitions. By performing ultrasound velocity measurements, we have obtained a detailed phase diagram with magnetic fields parallel and perpendicular to the triangular layers. The order of the phase transitions was found to be consistent with previous theoretical studies of generic two-dimensional triangular antiferromagnets. To support our experimental findings, we present a phenomenological model that includes biquadratic and next-nearest-neighbor interplane interactions. This model is sufficient to reproduce the phase diagram at low temperatures, and the next-nearest-neighbor interactions are shown to stabilize the incommensurate phases ($\mathbb{Y}$ and $\mathbb{V}$). Furthermore, the model provides insight regarding the magnetic ordering along the $\hat{c}$-axis in the magnetic plateau phase, suggesting that period 3 is established whenever the next-nearest-neighbor superexchange interactions are unequal. In the systems in which these interactions are expected to be equal, the model predicts degeneracy between period 2 and period 3 structures, at the classical level.

DOI: 10.1103/PhysRevB.103.224422

I. INTRODUCTION

Triangular-lattice antiferromagnets (TLAFs) are undoubtedly the simplest example of frustrated magnetic systems. However, they still provide a large playground for theoretical and experimental research due to their rich magnetic phase diagrams, which include both collinear and noncollinear magnetic phases. $RbFe(MoO_4)_2$ belongs to a crystalline family with the general formula $A^+R^{3+}(MO_4)_2$, where A is Ag, Tl, or an alkali metal; R is either a rare-earth atom, Bi, In, Ga, Al, Fe, or Cr; and M is either Mo or W. $RbFe(MoO_4)_2$ along with several other iron-containing molybdates, such as $CsFe(MoO_4)_2$ and $TlFe(MoO_4)_2$, all have trigonal structure with Fe^{3+} magnetic ions located on triangular networks, stacked directly on top of each other [1–3], making them excellent physical systems for studying the properties of quasi-two-dimensional TLAFs. A common feature of this family of materials is a structural phase transition at $T \leqslant 190$ K which changes the space group of the crystal from $P\bar{3}m1$ to $P\bar{3}$ [2,4,5]. This transition corresponds to a rotation of MoO_4^{2-} tetrahedrons around the crystallographic $\hat{c}$-axis (perpendicular to the triangular layers) in a way that establishes three distinct superexchange pathways between magnetic ions in different triangular planes [4]. The low-temperature crystal structure and the superexchange pathways are presented in Fig. 1. Two of these (labeled J_a and J_b) correspond to the interplane next-nearest-neighbor (NNN) interactions, and the remaining one (J_2) is the interplane nearest-neighbor (NN) interaction between the spins. The intraplane NN exchange interaction, J_1, has been determined to be the dominant coupling with the coupling constant $J_1 \approx 1$ K. Since it is practically impossible to individually determine the three interplane interactions (J_2, J_a, J_b), the "effective" interplane coupling was previously deduced to be $J_c \approx 0.008$ K [4,6].

Over the years, there have been multiple experimental studies of the field-induced magnetic phases in $RbFe(MoO_4)_2$ using various experimental techniques [6–11]. Consequently, the magnetic phase diagram corresponding to the field parallel to the basal plane of the triangular lattice is relatively well-established. This experimental phase diagram is consistent with theoretical models for a generic XYZ TLAF with weak interplane coupling [12–18]. The spin configurations associated with the low-temperature phase sequence observed with the field applied parallel (H_x) and perpendicular (H_z) to the basal plane are presented in Figs. 2(a) and 2(b). In the absence of a magnetic field, the spin structure corresponds to the 120° configuration. When the external field is oriented parallel to the triangular planes, the magnetic phases are all coplanar and correspond to, in the order of increasing magnetic field, the $\mathbb{Y}$-state, the $\mathbb{UUD}$-state (up-up-down state, or magnetization plateau), the $\mathbb{C}$-state, the $\mathbb{V}$-state, and the fully saturated ferromagnetic state. In the case of $RbFe(MoO_4)_2$, as illustrated in Fig. 2(a), the $\mathbb{Y}$-state and $\mathbb{V}$-state phases have been shown to be incommensurate along the $\hat{c}$-axis with the $\hat{z}$-component of the wave vector determined to be $q_z \approx 0.468$ [4,10].

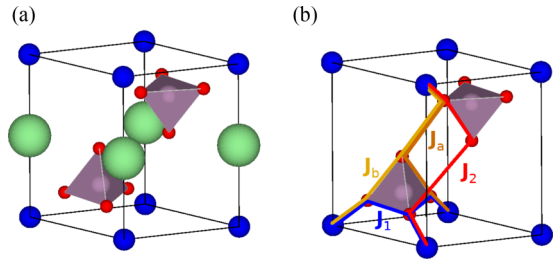

FIG. 1. (a) The low-temperature $P\bar{3}$ crystal structure of $RbFe(MoO_4)_2$. The superexchange interactions between the Fe^{3+} ions (blue) shown in (b) are mediated by the O^{2-} anions (red) located on the MoO_4^{2-} pyramids (purple). The Rb^+ ions (green) are nonmagnetic and do not contribute to the magnetic interactions.

Interestingly enough, the number of magnetic phases has been slightly inconsistent in the recent literature. In particular, a recent neutron study [4] reported the four above-mentioned magnetic phases, whereas previous ^{87}Rb-NMR [8], as well as heat capacity, magnetization, and dielectric measurements [7,9], clearly display five distinct phases, where the order of magnetic states follows that presented in Fig. 2(a) with an additional phase between the $\mathbb{Y}$-state and the $\mathbb{UUD}$-state. This new phase has the same spin structure as the $\mathbb{Y}$-state, except the spins in different layers completely overlap, leading to a commensurate order. Therefore, in the remainder of this work we will refer to this magnetic order as the commensurate $\mathbb{Y}$-state. Previous studies have also indicated that the magnetoelectric coupling may be responsible for stabilizing this new phase [7,9,10].

When the external field is applied perpendicular to the triangular layers [Fig. 2(b)], the 120° structure develops a small magnetization component in the $\hat{z}$-direction forming a

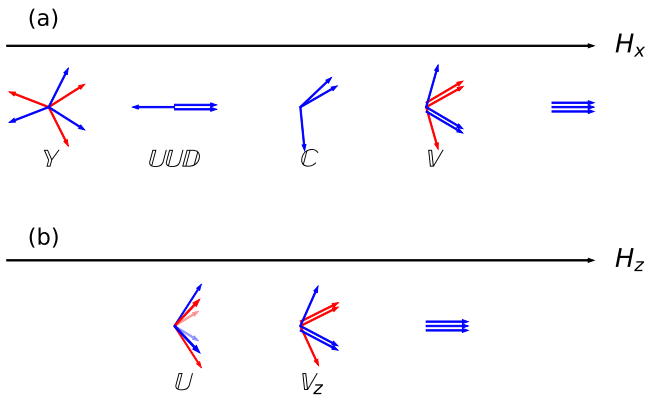

FIG. 2. Field dependence of low-temperature magnetic phases of TLAF with weak interplane interactions and applied fields parallel (a) and perpendicular (b) to the triangular layers. The spin arrows on different magnetic sublattices are drawn from the same origin for easier presentation. Blue and red arrows differentiate between spins in different triangular layers. For the $\mathbb{UUD}$, $\mathbb{V}$, $\mathbb{V}_z$, and saturated states, the overlapping spins are shifted for clarity. The black arrow indicates the relative magnitude (not to scale) and orientation of the external magnetic field. Note that in the case of the $\mathbb{U}$-state, the spins remain in a 120° configuration in the xy plane, but they also obtain a magnetization component along the z-axis.

noncoplanar $\mathbb{U}$-state (umbrella). As the magnitude of the field is increased, the spin structure is predicted to discontinuously change into the coplanar $\mathbb{V}_z$-state. Recently, the magnetic phase diagram of $RbFe(MoO_4)_2$ with applied field parallel to the $\hat{c}$ axis was constructed from polarization, dielectric susceptibility, and magnetization data [7,20]. The experimental results display two phases, in agreement with the numerical calculations for this field orientation [Fig. 2(b)] [21].

For both field orientations (parallel and perpendicular to the triangular layers), the order of phase transitions between low-field phases ($\mathbb{C}$-state and $\mathbb{U}$-state, respectively) and the $\mathbb{V}$-states has been inconsistent in the literature: the experimental results seem to indicate that these transitions are continuous [6–11], despite numerical work predicting first-order transitions [17–19]. Similar first-order transitions have been observed experimentally in other quasi-two-dimensional TLAFs, such as $BaCo_3Sb_2O_9$ [22].

Recent theoretical studies of weakly coupled TLAFs with additional biquadratic intraplane interactions [18], which are known to stabilize the magnetization plateau [23], revealed that even small interplane couplings are responsible for the stabilization of some magnetic phases (including the $\mathbb{C}$-state) at high fields. Therefore, one might expect that the addition of the biquadratic term, as well as the NNN interplane interactions, may stabilize incommensurate order, as reported in previous experimental studies [4,10].

In this paper, we aim to resolve some of these discrepancies in the literature by presenting high-resolution ultrasound velocity measurements of $RbFe(MoO_4)_2$. These results were used to construct detailed magnetic phase diagrams with the magnetic field parallel and perpendicular to the basal planes of the triangular layers. The order of the phase transitions was determined through the observation of hysteresis between the ascending and descending temperature and field sweeps. The phase transition between the incommensurate-commensurate $\mathbb{Y}$-states was not observed in the ultrasound velocity measurements. The reason for this could be that the acoustic wavelength is orders of magnitude larger than the interatomic distances, which might result in a reduced sensitivity to the incommensurate to commensurate types of phase transitions. Nevertheless, the observation of magnetic hysteresis at the phase boundary between the $\mathbb{C}$ and $\mathbb{V}$ states has made it clear that the phase transitions are of first order, in agreement with previous theoretical predictions. Similarly, the experimental results suggest that the phase transition between $\mathbb{U}$ and $\mathbb{V}_z$ phases is of first order. In addition to the experimental results, we also present a classical spin model, and we show that it is able to qualitatively reproduce the experimental phase diagrams at low temperatures. Importantly, the proposed model correctly predicts the magnetization plateau, and we are further able to show that unequal NNN interplane interactions ($J_a \neq J_b$) will always stabilize period 3 along the $\hat{c}$-axis in this phase.

The rest of the paper is organized as follows. Section II briefly describes the experimental procedure, and in Sec. III we confirm the existence of the first-order transitions for both field orientations by conducting high-resolution ultrasound velocity measurements, which we use to construct detailed phase diagrams for magnetic field parallel and perpendicular to the basal plane ($B \parallel ab$ and $B \parallel \hat{c}$, respectively).

In Sec. IV we present the classical Heisenberg model with intraplane biquadratic interactions. When the NNN interactions are unequal, the magnetic phases alternate between incommensurate and commensurate structures, in agreement with the previously reported neutron scattering results. The magnetization and spin structure for magnetic field parallel and perpendicular to the triangular planes are presented in Sec. V, and the analytical calculations for the magnetic ordering in the magnetization plateau phase are given in Sec. VI. Finally, the results of this work are summarized in Sec. VII.

II. EXPERIMENT

All experimental measurements were conducted on a thin plate single crystal (0.6 mm thick) grown by a spontaneous crystallization technique as described in [24]. Acoustic modes, propagating in the directions parallel and perpendicular to the triangular planes, were found to be well-coupled to the spin degrees of freedom and were used to determine the temperature–magnetic-field phase diagram of $RbFe(MoO_4)_2$. In the following, we set the velocity propagation axes such that the $\hat{z}$-axis is parallel to the crystallographic $\hat{c}$ axis. Due to the small dimensions of the sample, the alignment of the $\hat{x}$ and $\hat{y}$ axes with the in-plane crystallographic axes was not possible; however, this did not influence the experimental results since the elastic properties are isotropic in the directions parallel to the triangular layers. For modes propagating along the $\hat{z}$ axis, the sample was placed on a 2.46-mm-thick nonmagnetic CaF_2 buffer, and 30-MHz $LiNbO_3$ piezoelectric transducers were mounted to the corresponding faces of the crystal and the buffer. The first set of experiments was conducted at 90 MHz by measuring the velocity of the longitudinal mode, propagating along the $\hat{z}$-axis, $V_{L\hat{z}}$. For further investigations, transverse modes propagating and polarized in the basal plane were also measured, $V_{T\hat{x}P\hat{y}}$. In the latter case, the buffer was removed and the transducers were mounted normal to the triangular layers of the material. In both cases, the acoustic waves were generated by a high-precision pulsed acoustic interferometer in the transmission configuration giving a resolution of $\frac{\Delta V}{V} \sim 10^{-6}$. The measurements as a function of temperature and magnetic field were performed using a helium flow cryostat with an incorporated superconducting magnet. In this study, the temperature dependence was determined between 1.8 and 5 K with the magnetic field applied parallel and perpendicular to the triangular plane between 0 and 15 T.

III. EXPERIMENTAL RESULTS

A. Magnetic field parallel to the basal plane (B ∥ ab)

In Fig. 3, we present a series of experimental results for the relative velocity variation ($\frac{\Delta V}{V}$) as a function of the magnetic field. Both sets of velocity measurements ($V_{T\hat{x}P\hat{y}}$ and $V_{L\hat{z}}$) display three anomalies, as shown in Fig. 3, confirming the existence of magnetic phase transitions. Moreover, as presented in Fig. 3(c), we observed magnetic hysteresis loops characteristic of a first-order transition. Figure 4 shows the relative velocity variation as a function of temperature measured at different fields. As seen in Figs. 4(a) and 4(b),

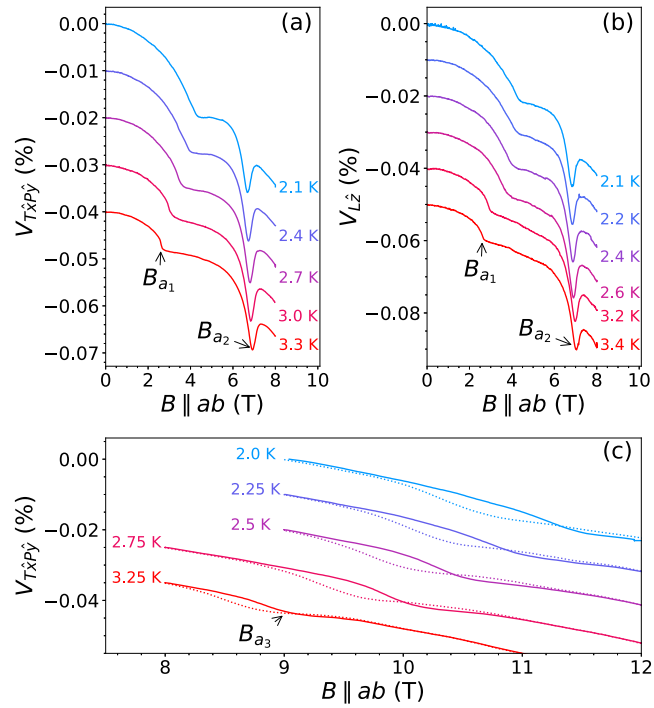

FIG. 3. Relative velocity variation as a function of magnetic field, $B \parallel ab$, for (a) transverse ($V_{T\hat{x}P\hat{y}}$) and (b) longitudinal ($V_{L\hat{z}}$) modes. (c) Field scans displaying magnetic hysteresis loops indicate a first-order transition. Solid lines are for increasing field, and dotted lines are for decreasing field. The individual scans are offset for clarity.

only one anomaly occurs at low fields. However, as the magnitude of the magnetic field increases, another anomaly appears between $B = 2.0$ and 2.3 T. These results for the relative velocity variation as a function of temperature and magnetic field were used to construct the temperature-field phase diagram of $RbFe(MoO_4)_2$ presented in Fig. 5. The general structure of this phase diagram is, for the most part, consistent with the previous experimental measurements. The Néel temperature at zero field, T_N, was determined to be $T_N = 3.64$ K, which is slightly lower than the value determined in previous reports ($T_N = 3.8$–3.9 K) [6–11]. Note also that the commensurate $\mathbb{Y}$-state (labeled as P2 in [10]) was not observed in the present experiment. Based on some of the previous experimental phase diagrams, we would expect this phase to fall between $B = 4$ and 5 T at $T = 2$ K with the phase boundaries quickly merging at higher temperatures [6,10]. The coexistence region between $\mathbb{C}$ and $\mathbb{V}$ (Fig. 5, dashed lines) phases was determined from the hysteresis appearing in the velocity data. The lower and upper boundaries of this region correspond, respectively, to scans with decreasing and increasing values of temperature or magnetic field.

B. Magnetic field perpendicular to the basal plane (B ∥ ĉ)

In Fig. 6 we present the representative data for the relative velocity variation with the magnetic fields parallel to the $\hat{c}$ axis. As before, both sets of velocity measurements

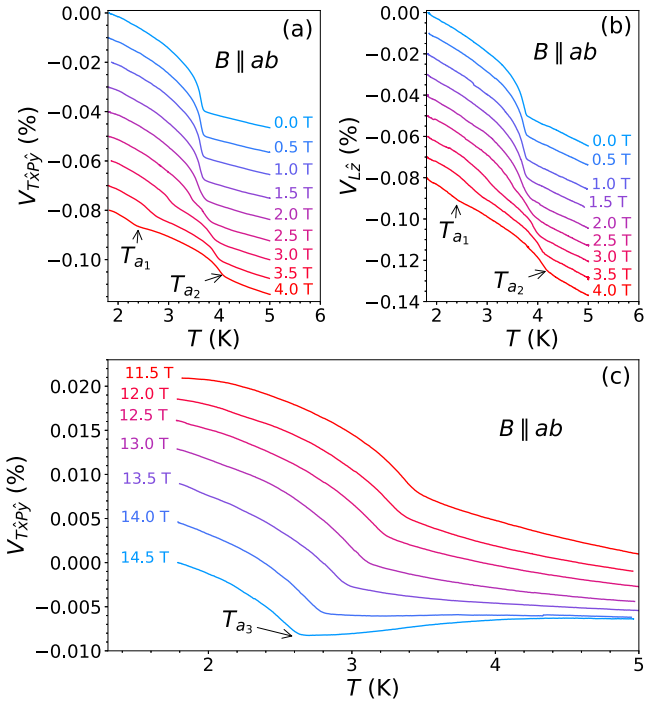

FIG. 4. Relative velocity variation of transverse modes propagating and polarized in the basal plane ($V_{T\hat{x}P\hat{y}}$) measured as a function of temperature with field parallel to the basal plane ($B \parallel ab$) (a,c) and longitudinal modes propagating along the $\hat{z}$ direction parallel to the crystallographic c-axis ($V_{L\hat{z}}$) (b). The low-field (0–4 T) results in (a) and (b) display two phase boundaries, and an additional high-field transition (11.5–14.5 T) is shown in (c).

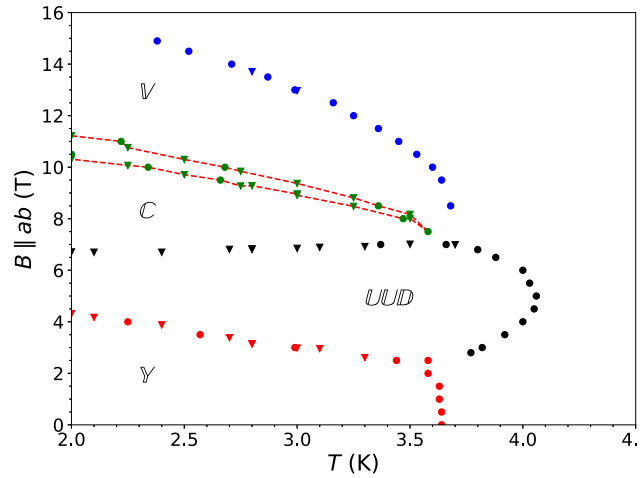

FIG. 5. Temperature-field experimental phase diagram of $RbFe(MoO_4)_2$ for $B \parallel ab$ obtained from sound velocity measurements of the transverse acoustic mode $V_{T\hat{x}P\hat{y}}$. Circles and triangles indicate temperature and field scans, respectively, and the dashed red lines indicate the coexistence region for the first-order transition.

display the same progression of anomalies as a function of temperature [Figs. 6(a)–6(c)]. The field scans with an increasing and decreasing field display clear hysteresis loops, demonstrating that the phase transition between the $\mathbb{U}$-(umbrella) and the $\mathbb{V}_z$-state is of first order. Similarly, the temperature scans show small but prominent hysteresis loop signatures at higher field values. Note that in the case of high-field temperature scans [Fig. 6(c)], the velocity variation was nearly flat, so the derivatives of data were used in order to detect the anomalies corresponding to the magnetic phase transitions. Figure 7 shows the temperature-field phase diagram of $RbFe(MoO_4)_2$ for $B \parallel \hat{c}$. The structure of this phase diagram is typical for XY TLAFs such as $Ba_3CoSb_2O_9$ and $CsCuCl_3$ [22,25].

IV. MODEL

In describing the ground state of an easy-plane quasi-two-dimensional TLAF material, the spin fluctuations were shown to be crucial in stabilizing the magnetization plateau at one-third of the magnetization saturation value [15]. Zhitomirsky [23] determined that this effect of spin fluctuations can be qualitatively modeled with a biquadratic term in the classical approach. The large value of the total spin on Fe^{3+} ions ($S = 5/2$) allows for a classical treatment of magnetism in $RbFe(MoO_4)_2$, therefore to describe the magnetic structure of easy-plane two-dimensional (2D) TLAFs, one can write the

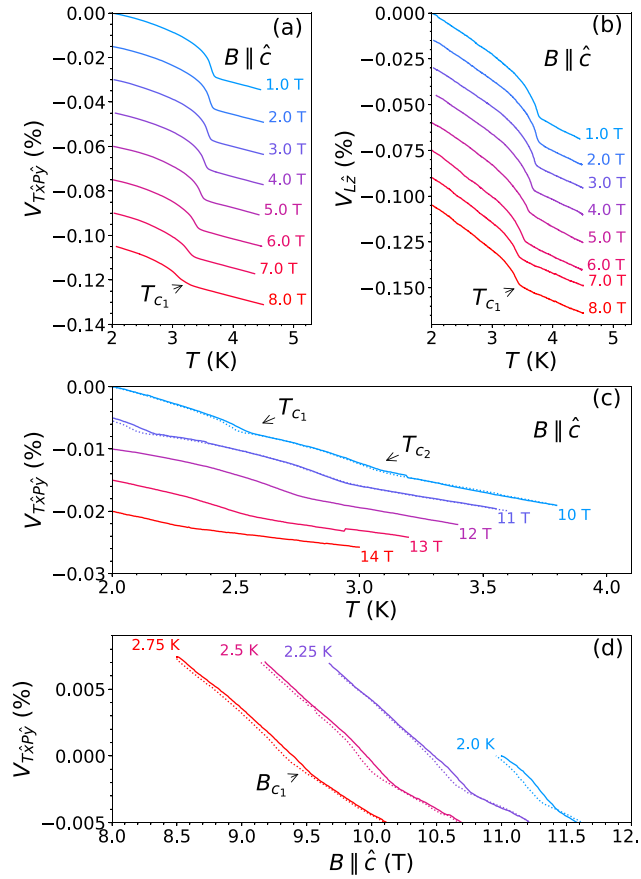

FIG. 6. Relative velocity variation as a function of (a)–(c) temperature scans at different fields, and (d) magnetic field scans at different temperatures for $B \parallel \hat{c}$. Solid and dotted lines in (c) and (d) denote increasing and decreasing values of temperature/field, respectively.

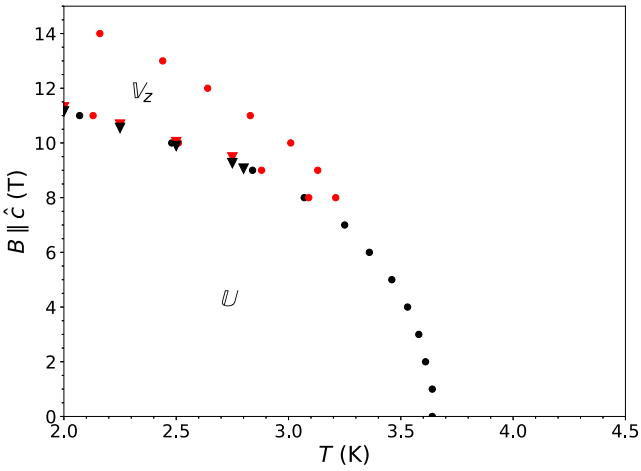

FIG. 7. Temperature-field experimental phase diagram of $RbFe(MoO_4)_2$ for $B \parallel \hat{c}$ obtained from sound velocity measurements in the transverse mode $V_{T\hat{x}P\hat{y}}$ as a function of temperature (circles) and field (triangles).

energy per plane using the following Heisenberg Hamiltonian with single-ion anisotropy:

$$\mathcal{H}_p = \mathcal{H}_p^{(J_1)} + \mathcal{H}_p^{(\gamma)} + \mathcal{H}_p^{(D)} + \mathcal{H}_p^{(Z)}, \tag{1}$$

$$\mathcal{H}_p^{(J_1)} = J_1 \sum_{\langle ij \rangle} \mathbf{S}_{i,p} \cdot \mathbf{S}_{j,p}, \tag{2}$$

$$\mathcal{H}_p^{(\gamma)} = -\gamma \sum_{\langle ij \rangle} (\mathbf{S}_{i,p} \cdot \mathbf{S}_{j,p})^2, \tag{3}$$

$$\mathcal{H}_p^{(D)} = D \sum_i \left(S_{i,p}^z\right)^2, \tag{4}$$

$$\mathcal{H}_p^{(Z)} = -\frac{1}{3}\mathbf{H} \cdot \sum_i \mathbf{S}_{i,p}, \tag{5}$$

where $\mathcal{H}_p^{(J_1)}$ is the isotropic exchange, $\mathcal{H}_p^{(\gamma)}$ is the phenomenological biquadratic exchange coupling, $\mathcal{H}_p^{(D)}$ is the single-ion anisotropy, and $\mathcal{H}_p^{(Z)}$ is the Zeeman interaction. Here, p labels the crystal plane, $J_1 > 0$ is the in-plane coupling constant, $\gamma < 0$ is the biquadratic coupling constant, $D > 0$ is the single-ion anisotropy constant, and $\mathbf{H}$ is the auxiliary magnetic field. Indices i, j indicate sites on the triangular lattice, and $\langle \cdots \rangle$ implies summation over nearest neighbors. In the classical approximation, the spins $\mathbf{S}_{i,p}$ are represented as continuous vectors rather than operators. This model successfully predicts four phases on the phase diagram: the $\mathbb{Y}$-state (with 120° configuration at $H = 0$), the $\mathbb{U}\,\mathbb{U}\,\mathbb{D}$-state (magnetization plateau), and the $\mathbb{V}$-state, which then leads to magnetic saturation. The results obtained with this classical 2D XY model at $T = 0$ are perfectly consistent with other approaches such as spin-wave theory [4]. However, Yamatoto *et al.* [17,19] recently showed that the inclusion of a weak antiferromagnetic interplane coupling in the Hamiltonian leads to an additional magnetic phase, the $\mathbb{C}$-state. Moreover, the calculations of Li *et al.* [18] indicate that the size of this interplane coupling may introduce an even larger variety of magnetic phases, radically changing the phase diagram. In $RbFe(MoO_4)_2$, NNN interplane interactions have also been shown to play a crucial role in stabilizing the incommensurate ground state at $H = 0$ [4,26,27]. Therefore, the energy per magnetic plane is written as

$$\mathcal{H} = \sum_p^N \frac{1}{N}\mathcal{H}_p + \frac{1}{N-1}\mathcal{H}_p^{(\mathrm{IPC})}, \tag{6}$$

where the interplane coupling is given by

$$\mathcal{H}_p^{(\mathrm{IPC})} = \sum_i J_2 \mathbf{S}_{i,p} \cdot \mathbf{S}_{i,p+1} + \sum_{\langle\langle ijk \rangle\rangle} J_a \mathbf{S}_{i,p} \cdot \mathbf{S}_{j,p+1} + J_b \mathbf{S}_{i,p} \cdot \mathbf{S}_{k,p+1}. \tag{7}$$

Here, N is the number of magnetic planes. Indices i, j, and k label the sites on the triangular layers, and $\langle\langle \cdots \rangle\rangle$ implies summation over interplane NNN, as presented in Fig. 1. J_2 represents the interplane NN coupling constant, while J_a and J_b correspond to two different NNN interplane coupling constants. In this work, we set $J_1 = 1$ thus normalizing the magnitudes of the remaining interactions with respect to the in-plane exchange. Using the values from Ref. [4], we also set $D/J_1 = 0.31$ and $J_2/J_1 = 0.008$. Li *et al.* [18] showed that the value of $\gamma/J_1 = -0.05$ can successfully reproduce the magnetization plateau. Furthermore, Li *et al.* [18] also showed that for $0 < J_2/J_1 < 0.1$, the z-components of the spins $S_{i,p}^z = 0$. Therefore, we parametrize the spins as two-dimensional vectors:

$$\mathbf{S}_{i,p} = (\cos\theta_{i,p}, \sin\theta_{i,p}). \tag{8}$$

Minimizing the energy with respect to the angles $\theta_{i,p}$, the solution for the spin configuration of the system is obtained at various magnetic fields. The ground state ($H = 0$) can be determined by treating the interplane coupling as a perturbation and assuming a 120° state for each plane. This amounts to only considering three sites in each plane (a single triangular unit), which reduces Eq. (6) to an equation with a single variable, q_z, which is the z-component of the magnetic wave vector,

$$\mathcal{H}_{120} = \frac{3\gamma}{4} - \frac{3}{2} + 3J_2\cos 2\pi q_z + \frac{3}{2}J_a(\sqrt{3}\sin 2\pi q_z - \cos 2\pi q_z) - \frac{3}{2}J_b(\sqrt{3}\sin 2\pi q_z + \cos 2\pi q_z). \tag{9}$$

The solution obtained by minimizing the magnetic energy corresponds to

$$2\pi q_z = -\arctan\left(\frac{\sqrt{3}(J_b - J_a)}{2J_2 - (J_a + J_b)}\right) + \pi. \tag{10}$$

The values of q_z are plotted as a color map in Fig. 8. Note that when one of J_a and J_b is 0, the value of q_z becomes 1/3 or 2/3, which both correspond to period 3 [28]. At the same time, whenever $J_a = J_b$, period 2 is favored.

Equation (10) allows us to determine the ratio between J_a and J_b by fixing q_z to the experimental value of $q_z = 0.468$. For further calculations, we used the values $J_a = 0.004$ and $J_b = 0.0048$ to minimize the magnetic energy for the range of magnetic field values ($H = 0$–10).

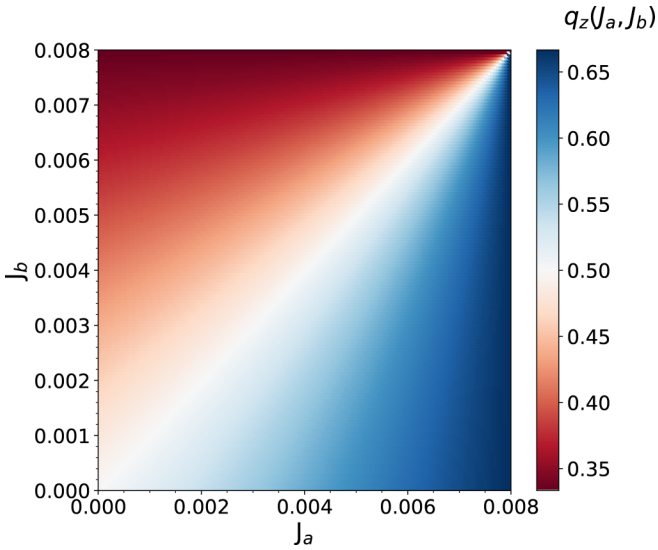

FIG. 8. q_z as a function of J_a and J_b corresponding to the second solution in Eq. (10). The values on the color bar range from $q_z = 1/3$ to $2/3$.

V. MAGNETIZATION AND SPIN STRUCTURE

A. Magnetic field parallel to the basal plane ($\mathbf{H}_x$)

First, the calculations were performed for a system with only two planes. Using two planes allows one to establish periodic conditions along the $\hat{c}$-axis, without putting implicit constraints on the value of q_z. This allows for both commensurate and incommensurate solutions. Minimizing the energy, we calculate the ground-state spin configuration for each value of the magnetic field. The uniform magnetization of the system, $\mathbf{m} = \frac{1}{N_t}\sum_i \mathbf{S}_i$, where N_t is the total number of spins, gives a good representation of the magnetic structure of the system, and in particular it can be used to locate the magnetic phase transitions [29]. Figure 9 shows the calculated induced magnetization per spin as well as its derivative with respect to the applied field. These results display four phase transitions

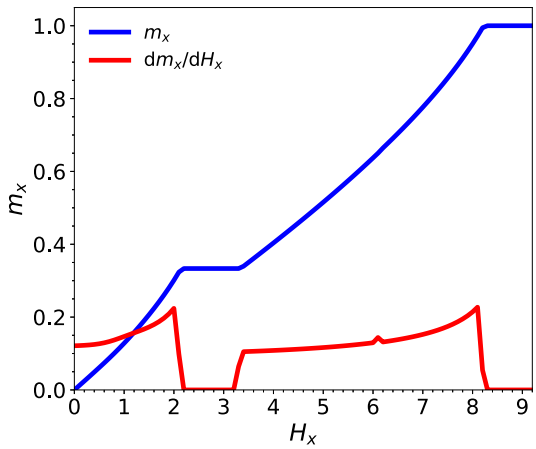

FIG. 9. Calculated magnetization (m_x) and its derivative ($\frac{dm_x}{dH_x}$) of $RbFe(MoO_4)_2$ per magnetic Fe^{3+} ion as a function of the applied magnetic field.

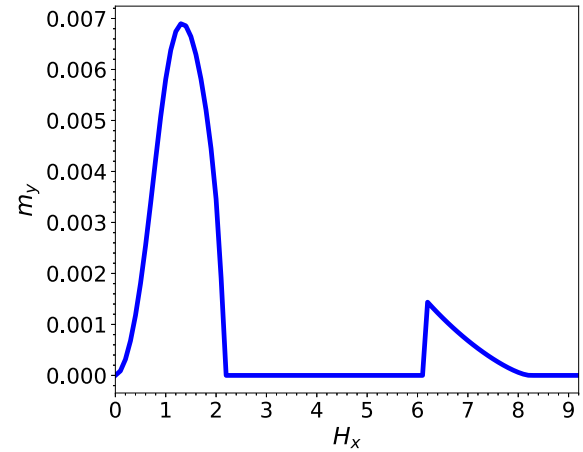

FIG. 10. The magnitude of the y-component of magnetization per plane.

with the transition points at $H \approx 2.2$, 3.2, 6.1, and 8.3. In agreement with Fig. 2(a), the five magnetic phases correspond to the $\mathbb{Y}$-state, the $\mathbb{UUD}$-state, the $\mathbb{C}$-state, the $\mathbb{V}$-state, and the saturated phase. The magnetization plateau ($\mathbb{UUD}$-state) at 1/3 of the magnetic saturation is a characteristic feature of the TLAFs. In addition to the induced magnetization parallel to the magnetic field, in incommensurate phases we also identified a small alternating transverse component of magnetization which on average cancels in the whole system. Figure 10 shows the magnitude of the transverse magnetization component (m_y) as a function of the applied magnetic field. As seen from this figure, the transverse magnetization is present in the $\mathbb{Y}$ state, then it vanishes in the plateau phase, and it reappears again in the $\mathbb{V}$ phase. The number and the order of these magnetic phases is consistent with the experimental observations, as described by the experimental phase diagram in Fig. 5. As mentioned above, the numerical results suggest that the transition between $\mathbb{C}$ and $\mathbb{V}$ phases is discontinuous, implying a first-order transition, which is consistent with the sound velocity data as shown in Fig. 3.

Next, we study the stabilization energy of the incommensurate order by adding another magnetic plane and imposing the periodic boundary conditions, which imposes a period 3 order. Labeling the energies of two- and three-layer systems as E_2 and E_3, respectively, the energy difference $\Delta E = E_2 - E_3$ between the two systems (Fig. 11) is small for all fields, however these results display a clear field dependence. In particular, the difference in energy is zero in the phases where we expect a period 3 commensurate order and is negative in the incommensurate phases observed in the system with two planes. Therefore, in general, $\Delta E \leqslant 0$ or $E_2 \leqslant E_3$. As mentioned earlier, a system with two magnetic planes allows for both commensurate and incommensurate structures, however in the case of three planes, the periodic boundary conditions effectively fix the period of the system at 3. From previous neutron scattering results, the z-component of the magnetic wave vector $\mathbf{Q}$ is $q_z \approx 0.468$ for incommensurate structures and $q_z = 1/3$ for the commensurate states. Therefore, our results show, in agreement with the neutron scattering experiments, that the incommensurate phases predicted with two planes give a true ground state as compared to the period 3

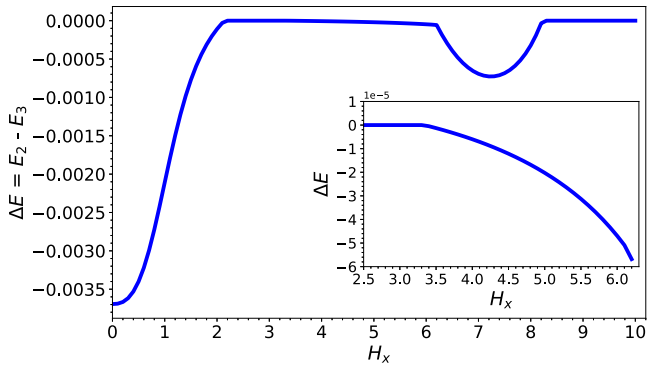

FIG. 11. Field dependence of the energy difference between a system with two planes and a system with three planes and periodic boundary conditions: $\Delta E = E_2 - E_3$. A system with two planes allows for commensurate and incommensurate solutions, while a system with three planes and periodic conditions constrains the periodicity along $\hat{c}$ to period 3. The inset shows a zoomed-in region near the transition between the UUD and the $\mathbb{V}$ phases. Small nonzero component of ΔE may indicate weak incommensurate nature of the $\mathbb{C}$-state.

structures imposed by the periodic conditions in a system with three planes ($E_2 < E_3$). For the commensurate states, both systems predict the same ordering, thus $\Delta E = 0$. Notably, the energy difference is slightly less than zero for the $\mathbb{C}$ phase, as shown in the zoomed-in window in Fig. 11. This indicates that this phase might be weakly incommensurate; however, since the magnitude ΔE is very small, these speculations require stronger evidence before any conclusions are drawn.

B. Magnetic field parallel to the basal plane ($\mathbf{H}_z$)

To analyze the system with the applied field along the $\hat{c}$ axis, the spins are rewritten in spherical coordinates to include the z-component:

$$\mathbf{S}_{i,p} = (\cos\phi_{i,p}\sin\theta_{i,p}, \sin\phi_{i,p}\sin\theta_{i,p}, \cos\theta_{i,p}), \tag{11}$$

where $\phi_{i,p}$ and $\theta_{i,p}$ represent the azimuthal and polar angles of the ith spin in the pth plane. The physical properties of the system can therefore be calculated by minimizing the Hamiltonian with respect to these spin coordinates. The uniform magnetization along the z-axis (m_z) as well as its derivative ($\frac{dm_z}{dH_z}$) are presented in Fig. 12 as a function of the magnetic field. In total, Fig. 12 displays two phase transitions at $H \approx 8.0$ and 10.1. The spin configurations for these three phases, in agreement with Fig. 2(b), correspond to the $\mathbb{U}$-state (Umbrella), the $\mathbb{V}_z$-state, and the saturated phase.

VI. MAGNETIC ORDER IN THE MAGNETIZATION PLATEAU

Another interesting observation from Fig. 11 is that in the UUD phase, the energies for periods 2 and 3 are the same, despite the fact that the experimental results for $RbFe(MoO_4)_2$ [4,10] clearly indicate that $q_z = 1/3$ in the magnetization plateau. This can be understood by considering the spin configurations for periods 2 and 3 in the magnetization plateau, as depicted in Fig. 13. If only the first two planes are considered,

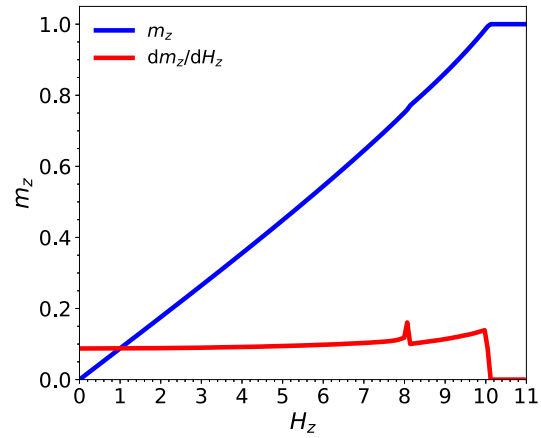

FIG. 12. Numerically calculated magnetization of $RbFe(MoO_4)_2$ per magnetic Fe^{3+} ion and its derivative as a function of the magnetic field applied along the $\hat{c}$ axis.

the spin configuration is exactly the same, which implies that for a system with two planes, periods 2 and 3 are degenerate, explaining the results in Fig. 11. As a matter of fact, periods 2 and 3 are the only two possible long-range antiferromagnetic periodic configurations along the z-axis in the UUD phase. For both of these cases, the magnetic energies can be written by using Eq. (6) for six planes with periodic conditions by imposing the corresponding spin structures:

$$E_{p2} = -J_2 + J_a + J_b + 3\gamma - 2, \tag{12}$$

$$E_{p3} = -J_2 + 3\gamma - 2 + \begin{cases} -J_b + 3J_a & \text{if } J_b > J_a, \\ -J_a + 3J_b & \text{if } J_a > J_b. \end{cases} \tag{13}$$

Using six planes and periodic boundaries ensures that both periods 2 and 3 are allowed, as discussed previously. Using Eqs. (12) and (13), the energy difference can be calculated to

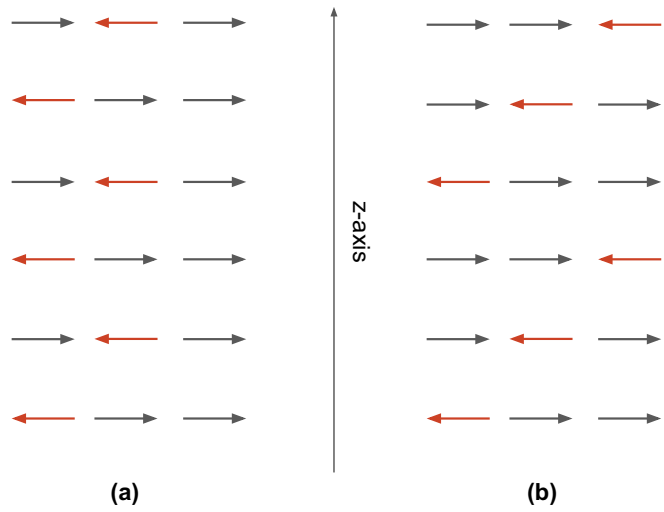

FIG. 13. Spin ordering for six planes in the UUD phase. The three spins in a triangle are placed next to each other for better presentation. Period 2 (a) corresponds to $q_z = 1/2$ for two of the spins and $q_z = 0$ for another. On the other hand, period 3 (b) implies $q_z = 1/3$ for all three spins.

determine the ground state:

$$\Delta E = E_{p3} - E_{p2} = \begin{cases} 2J_a - 2J_b & \text{if } J_b > J_a, \\ 2J_b - 2J_a & \text{if } J_a > J_b. \end{cases} \quad (14)$$

In both cases, $\Delta E < 0$ implying that $E_{p3} < E_{p2}$ for all values of γ, J_2, J_a, and J_b. Hence, period 3 is favored whenever $J_a \neq J_b$. Svistov *et al.* in Ref. [7] previously calculated that the dipolar interactions may also lift the degeneracy making period 3 structure slightly more favorable, however the corresponding energy contribution is an order of magnitude smaller than that due to the NNN exchange interactions presented in this work. It remains unclear, however, if either period 2 or 3 would be stabilized if $J_a = J_b$, since the classical model predicts that in this case the two states would be degenerate. Experimentally, $Ba_3CoSb_2O_9$ is known to have a period 2 structure in the magnetization plateau [30]. The hexagonal symmetry of this material (in particular, the sixfold rotations) ensures that $J_a = J_b$. This poses a problem since, as mentioned above, periods 2 and 3 are predicted to be degenerate in this system; however, the experimental results suggest that other factors stabilize the period 2 configuration. The methods used in this work are restricted to the energy calculations, so a more sophisticated model is required in order to study the stability of period 2 and period 3 states for this system.

VII. CONCLUSIONS

In this work, we were able to experimentally confirm the nature of the magnetic phase transitions in $RbFe(MoO_4)_2$ with magnetic fields oriented parallel and perpendicular to the triangular layers. The phase transitions between the $\mathbb{C}$ and $\mathbb{V}$ states, as well as the $\mathbb{U}$ and $\mathbb{V}_z$ states, were confirmed to be of first order, in agreement with previous theoretical predictions. The ultrasound velocity measurements only show one of the previously reported $\mathbb{Y}$ states (which corresponds to P1 in [10]). This is likely due to the fact that in the ultrasound velocity measurements, the acoustic wavelength is large compared to the interatomic distances, which implies that the measurements are sensitive to the changes in the order parameters averaged over many unit cells of the crystal. Since only the q_z changes in the transition between the incommensurate and commensurate $\mathbb{Y}$-states (i.e., no considerable change in spin polarization), it is reasonable to speculate that this transition cannot be resolved in the ultrasound velocity experiment. On the contrary, the transition between the $\mathbb{C}$ and $\mathbb{V}$ phases is very well defined since in addition to the change in q_z there is also a discontinuous change in the spin structure of each spin triangle where two of the spins become parallel.

The phenomenological model presented in this paper is sufficient to reproduce the phase diagram at low temperatures. The unequal NNN interplane interactions were shown to stabilize the incommensurate phases ($\mathbb{Y}$ and $\mathbb{C}$). These results generalize previously studied models where crystal symmetry implies $J_a = J_b$ (in materials such as $Ba_3CoSb_2O_9$), and only commensurate phases are allowed. As with the experimental results, our model does not predict the commensurate $\mathbb{Y}$-state since we did not include the magnetoelectric coupling which was shown to stabilize this magnetic phase [10].

Lastly, we were able to show that unequal NNN interactions favor period 3 in the magnetic plateau, which is supported by previous neutron diffraction studies [4]. Furthermore, in the systems in which $J_a = J_b$, the model predicts the energies of the UUD structures with periods 2 and 3 to be the same, however the neutron diffraction studies [30] indicate that period 2 is the equilibrium spin configuration in $Ba_3CoSb_2O_9$. As a result, there must be higher-order effects, not accounted by our model, which stabilize one configuration over another.

ACKNOWLEDGMENTS

The authors would like to thank O. A. Petrenko, A. I. Smirnov, and M. L. Plumer for very valuable discussions and suggestions. We also acknowledge extensive technical support from M. Castonguay. This work was supported by the Natural Sciences and Engineering Research Council of Canada (NSERC).

[1] M. Maczka, A. G. Souza Filho, W. Paraguassu, P. T. C. Freire, J. Mendes Filho, and J. Hanuza, Prog. Mater. Sci. **57**, 1335 (2012).
[2] A. Gaągor, P. Zajdel, and D. Többens, J. Alloys Compd. **607**, 104 (2014).
[3] A. V. Sobolev, E. S. Kozlyakova, I. S. Glazkova, V. A. Morozov, E. A. Ovchenkov, O. S. Volkova, A. N. Vasiliev, N. S. Ovanesyan, Y. M. Kadyrova, E. G. Khaikina, K. Molla, B. Rahaman, T. Saha-Dasgupta, S. Kamusella, H.-H. Klauss, and I. A. Presniakov, J. Phys. Chem. C **122**, 19746 (2018).
[4] J. S. White, C. Niedermayer, G. Gasparovic, C. Broholm, J. M. S. Park, A. Y. Shapiro, L. A. Demianets, and M. Kenzelmann, Phys. Rev. B **88**, 060409(R) (2013).
[5] M. Maczka, K. Hermanowicz, P. E. Tomaszewski, and J. Hanuza, J. Phys.: Condens. Matter **16**, 3319 (2004).
[6] L. E. Svistov, A. I. Smirnov, L. A. Prozorova, O. A. Petrenko, L. N. Demianets, and A. Y. Shapiro, Phys. Rev. B **67**, 094434 (2003).
[7] L. E. Svistov, A. I. Smirnov, L. A. Prozorova, O. A. Petrenko, A. Micheler, N. Büttgen, A. Y. Shapiro, and L. N. Demianets, Phys. Rev. B **74**, 024412 (2006).
[8] L. E. Svistov, L. A. Prozorova, N. Büttgen, A. Y. Shapiro, and L. N. Dem'yanets, J. Exp. Theor. Phys. Lett. **81**, 102 (2005).
[9] H. Mitamura, R. Watanuki, N. Onozaki, Y. Shimura, S. Kittaka, T. Sakakibara, and K. Suzuki, J. Phys.: Conf. Ser. **391**, 012099 (2012).
[10] H. Mitamura, R. Watanuki, K. Kaneko, N. Onozaki, Y. Amou, S. Kittaka, R. Kobayashi, Y. Shimura, I. Yamamoto, K. Suzuki, S. Chi, and T. Sakakibara, Phys. Rev. Lett. **113**, 147202 (2014).
[11] A. I. Smirnov, T. A. Soldatov, O. A. Petrenko, A. Takata, T. Kida, M. Hagiwara, A. Y. Shapiro, and M. E. Zhitomirsky, Phys. Rev. Lett. **119**, 047204 (2017).
[12] H. Kawamura and S. Miyashita, J. Phys. Soc. Jpn. **54**, 4530 (1985).
[13] S. E. Korshunov, J. Phys. C **19**, 5927 (1986).

[14] M. L. Plumer and A. Caillé, Phys. Rev. B **42**, 10388 (1990).
[15] A. V. Chubukov and D. I. Golosov, J. Phys.: Condens. Matter **3**, 69 (1991).
[16] D. H. Lee, J. D. Joannopoulos, J. W. Negele, and D. P. Landau, Phys. Rev. B **33**, 450 (1986).
[17] D. Yamamoto, G. Marmorini, and I. Danshita, J. Phys. Soc. Jpn. **85**, 024706 (2016).
[18] M. Li, M. L. Plumer, and G. Quirion, J. Phys.: Condens. Matter **32**, 135803 (2020).
[19] D. Yamamoto, G. Marmorini, and I. Danshita, Phys. Rev. Lett. **114**, 027201 (2015).
[20] H. Mitamura, R. Watanuki, N. Onozaki, Y. Amou, Y. Kono, S. Kittaka, Y. Shimura, I. Yamamoto, K. Suzuki, and T. Sakakibara, J. Magn. Magn. Mater. **400**, 70 (2016).
[21] S. Watarai, S. Miyashita, and H. Shiba, J. Phys. Soc. Jpn. **70**, 532 (2001).
[22] G. Quirion, M. Lapointe-Major, M. Poirier, J. A. Quilliam, Z. L. Dun, and H. D. Zhou, Phys. Rev. B **92**, 014414 (2015).
[23] M. E. Zhitomirsky, J. Phys.: Conf. Ser. **592**, 012110 (2015).
[24] R. F. Klevtsova and P. V. Klevtsov, Kristallografiya **15**, 953 (1970).
[25] A. Sera, Y. Kousaka, J. Akimitsu, M. Sera, T. Kawamata, Y. Koike, and K. Inoue, Phys. Rev. B **94**, 214408 (2016).
[26] A. J. Hearmon, F. Fabrizi, L. C. Chapon, R. D. Johnson, D. Prabhakaran, S. V. Streltsov, P. J. Brown, and P. G. Radaelli, Phys. Rev. Lett. **108**, 237201 (2012).
[27] K. Cao, R. D. Johnson, F. Giustino, P. G. Radaelli, G.-C. Guo, and L. He, Phys. Rev. B **90**, 024402 (2014).
[28] The z-component of the magnetic **Q**-vector is then either $\frac{2\pi}{3}$ or $\frac{4\pi}{3}$, which correspond to counterclockwise and clockwise rotations by $\frac{2\pi}{3}$, and thus describe period 3 along the z-axis.
[29] A. I. Smirnov, H. Yashiro, S. Kimura, M. Hagiwara, Y. Narumi, K. Kindo, A. Kikkawa, K. Katsumata, A. Y. Shapiro, and L. N. Demianets, Phys. Rev. B **75**, 134412 (2007).
[30] Y. Kamiya, L. Ge, T. Hong, Y. Qiu, D. L. Quintero-Castro, Z. Lu, H. B. Cao, M. Matsuda, E. S. Choi, C. D. Batista, M. Mourigal, H. D. Zhou, and J. Ma, Nat. Commun. **9**, 2666 (2018).